

1
2 **Spatiotemporal correlation analysis of noise-derived seismic body waves with ocean**
3 **wave climate and microseism sources**

4
5 **Lei Li¹, Pierre Boué¹, Lise Retailleau², Michel Campillo¹**

6 ¹Univ. Grenoble Alpes, Univ. Savoie Mont Blanc, CNRS, IRD, IFSTTAR, ISTerre, 38000
7 Grenoble, France

8 ²Observatoire Volcanologique du Piton de la Fournaise, IPGP, CNRS, UMR 7154-Sismologie,
9 La Plaine des Cafres, La Réunion, France

10
11 Corresponding author: Lei Li (ll.ynyf@gmail.com)

12
13 **Key Points:**

- 14 • Time variations of a noise-derived P -type phase are compared with those of the ocean
15 wave heights and microseism sources at a global scale.
- 16 • The correlation between the noise-derived phase and ocean wave height, is higher in the
17 surrounding regions than in the effective source region.
- 18 • We hint not to equate a positive correlation with a causal relation when studying the links
19 between noise sources and noise-derived signals.
- 20
21

22 Abstract

23 Seismic signals can be extracted from ambient noise wavefields by the correlation technique.
 24 Recently, a prominent P -type phase in the secondary microseism period band was observed from
 25 teleseismic noise correlations. The phase is named P_{dmc} in this paper, corresponding to its origin
 26 from the interference between the Direct P waves transmitting through the deep Mantle and the
 27 Core (P and $PKPab$ waves). The two correlated seismic networks are deployed in the north
 28 hemisphere. The microseism sources that are efficient for the P_{dmc} construction, locate in the
 29 south Pacific. We investigate the spatiotemporal links of the P_{dmc} signal with the global oceanic
 30 wave climate and microseism sources. Interestingly, the correlation with wave height is higher in
 31 several regions surrounding the effective source region, rather than in the effective source region.
 32 The P_{dmc} amplitude is highly correlated with the power of the effective microseism sources.
 33 Also, it is apparently correlated with ineffective sources in the southern hemisphere, and anti-
 34 correlated with sources in the north hemisphere. We ascribe the correlation with the ineffective
 35 southern sources to the spatiotemporal interconnections of the southern sources, which warns not
 36 to equate a positive correlation with a causal relationship. The anti-correlation with northern
 37 sources can be explained by the reverse seasonal patterns between the southern and northern
 38 sources, and by that the northern sources impede the signal construction. The signal construction
 39 from noise correlations relies on the competition between the effective and ineffective sources,
 40 not just on the power of the effective sources.

41

42 Plain Language Summary

43 Every place on the Earth planet is experiencing tiny but incessant microseisms induced by
 44 formidable natural forces, particularly, storm-driven ocean waves. The ambient microseism noise
 45 was deemed a nuisance, but now can be turned into signals via the seismic correlation technique.
 46 Recently, a P -type phase was derived from the noise correlations between two regional seismic
 47 networks. The noise-derived phase originates from the correlation between the direct P waves
 48 transmitting through the deep mantle and outer core of the Earth. The temporal variations in the
 49 amplitudes of the noise-derived signals are compared with the variations in the power of
 50 microseism sources in global oceans, to understand the links between the noise-derived signals
 51 and microseism sources. The results show that the signal construction depends on the
 52 competition of the sources that contribute to the signals with other sources. The conclusion can
 53 be generalized to other noise-derived seismic phases. We also analyze the links of the noise-
 54 derived signals to wave climate. In our case, the ocean waves in the contributing source region
 55 are dominated by wind waves, whereas the excitation of microseisms is primarily owing to
 56 swells generated by oceanic storms in surrounding regions.

57

58 1 Introduction

59 As early as the birth of seismometers in the later 19th century, the incessant background
 60 vibrations of Earth had been observed (Bernard, 1990; Dewey & Byerly, 1969; Ebeling, 2012).
 61 They were termed “microseisms” due to their feebleness. With more apparatus deployed
 62 worldwide, it was soon recognized that microseisms are ubiquitous and irrelevant to seismicity.
 63 The observation of microseisms aroused interests from various disciplines. Researchers linked
 64 the generation of microseisms to atmosphere processes and ocean wave activities. Meteorologists

65 tried to employ land observations of microseisms to track remote oceanic storms (e.g., Harrison,
66 1924). To the mid-twentieth century, it has been known well that microseisms are excited by
67 storm-driven ocean waves. The most energetic microseisms that dominate the seismic noise
68 spectra, namely, the so-called secondary microseisms at seismic periods around 7 s (Peterson,
69 1993), are excited by the nonlinear interactions between nearly equal-frequency ocean waves
70 propagating in nearly opposite directions (Longuet-Higgins, 1950; Hasselmann, 1963). The
71 periods of the excited secondary microseisms are half those of the colliding ocean waves. By
72 coupling the excitation theory of secondary microseisms proposed by Longuet-Higgins (1950)
73 with the ocean wave action model, Kedar et al. (2008) modeled the secondary microseism
74 excitations in the north Atlantic, and validated the numerical modeling by comparing with inland
75 seismological observations. Afterwards, more authors simulated the oceanic microseism sources
76 and some reported the consistency between predictions and observations (e.g., Ardhuin et al.,
77 2011, 2015; Hillers et al., 2012; Stutzmann et al., 2012; Nishida and Takagi, 2016).

78 The seismic excitation by an oceanic microseism source is essentially akin to that by an
79 earthquake, in that the seismic wavefield recorded at any point is a convolution of the source
80 time function with the Green function of the propagating medium between source and receiver.
81 Their main difference lies in the source process. For earthquakes, the sudden rupture of faults
82 leads to short-duration, impulsive source time functions. Isolated seismic phases are generally
83 distinguishable from the seismograms. In contrast, the excitation of microseisms, approximated
84 as Gaussian random process by some authors (Peterson, 1993; Steim, 2015), is incessant, leading
85 to long, random-like source time functions. The convolution mixture signals are not directly
86 discernible from the seismograms. With array beamforming (Rost & Thomas, 2002) or
87 correlation technique (Campillo & Paul, 2003; Shapiro & Campillo, 2004), specific phases from
88 distant microseism sources have been identified from microseism noise records (e.g., Gerstoft et
89 al., 2008; Landès et al., 2010; Zhang et al., 2010; Euler et al., 2014; Liu et al., 2016; Nishida &
90 Takagi, 2016; Meschede et al., 2017, 2018; Retailleau & Gualtieri, 2019). The correlation
91 technique is advantageous in that, by correlating the noise records at two receivers, explicit
92 seismic signals can be derived. Noise-derived surface waves have been used to infer the
93 azimuthal and seasonal changes of noise sources (e.g., Stehly et al., 2006). Noise-derived body
94 waves can provide better constrains in imaging the noise sources (Landès et al., 2010). Recently,
95 deep body waves that pass through the mantle and core have been extracted from ambient noise
96 (e.g., Boué et al., 2013; Lin et al., 2013; Nishida, 2013; Poli et al., 2015; Xia et al., 2016; Spica
97 et al., 2017). The noise-derived body waves are valuable for surveying the deep structure and for
98 understanding the links between seismological observations and atmospheric/oceanographic
99 phenomena.

100 Hillers et al. (2012) made the first global-scale comparison between the oceanic
101 microseism sources derived from seismological observations and oceanographic modeling. The
102 seismologically derived data (time resolution: 13 days; spatial resolution: 2.5° latitude \times 5°
103 longitude) are the global back-projections of near-zero-lag P signals generated from the cross
104 correlations of microseism P waves at seismic array (Landès et al., 2010). The modeled data
105 (time resolution: 3 hours; spatial resolution: 1° latitude \times 1.25° longitude) are a global extension
106 of the numerical simulation by Kedar et al. (2008). The two datasets are resampled to common
107 resolutions for comparison. For the seismologically derived data, the back-projection is based on
108 the relationship between the source-receiver distance and the horizontal slowness of teleseismic
109 P wave. However, seismic phases that have common slownesses (e.g., P and PP waves) cannot

110 be discriminated in this method (Gerstoft et al., 2008; Landès et al., 2010). Thus, the imaged
 111 sources are somewhat ambiguous. For the modeled data, coastal reflections of ocean waves, that
 112 can play a role in the ocean wave-wave interactions at near-coast regions (Longuet-Higgins,
 113 1950; Ardhuin et al., 2011), are neglected. Due to the resonance of seismic waves in the water
 114 columns, bathymetry can have significant effect on the excitation of microseisms (Longuet-
 115 Higgins, 1950; Kedar et al., 2008; Hillers et al., 2012). The importance to account for the
 116 bathymetric effect on the microseism P -wave excitations has been addressed in several studies
 117 (e.g., Euler et al., 2014; Meschede et al., 2017). Hillers et al. (2012) considered the bathymetric
 118 effect, but using the amplification factors derived by Longuet-Higgins (1950) for surface waves.

119 Rascle and Ardhuin (2013) established an oceanographic hindcast database that includes
 120 global oceanic secondary microseism sources of a 3-hour time resolution and a 0.5° spatial
 121 resolution. Coastal reflections were accounted for in the modeling (Ardhuin et al., 2011).
 122 Regarding the bathymetric effect on microseism excitations, Gaultieri et al. (2014) proposed the
 123 formulae for body waves based on ray theory. Concerning the localization of noise sources, Li et
 124 al. (2020) developed a double-array method that can estimate the respective slownesses of the
 125 interfering waves at the two correlated seismic arrays, and thereby, provide better constrains for
 126 the determination of the correlated seismic phases. The microseism sources that are effective for
 127 the derivation of the signals from seismic noise records, can be mapped by back-projecting the
 128 noise-derived signals along the ray paths of the correlated phases. The double-array
 129 configuration eliminates the ambiguity in determining the effective source region (Fresnel zone).
 130 In this study, we integrate these new progresses to survey the associations of noise-derived body
 131 waves to ocean wave activities and microseism excitations.

132 The paper is organized as follows. In section 2, we review the main results of Li et al.
 133 (2020) who reported the observation of a prominent P -type phase from the noise correlations
 134 between two regional seismic networks at teleseismic distance. The noise-derived phase has its
 135 spectral content concentrated in the period band of the secondary microseisms that are excited by
 136 the nonlinear ocean wave-wave interactions. In this paper, we denote the phase as P_{dmc} ,
 137 corresponding to the fact that the phase originates from the correlation between the Direct P
 138 waves that transmit through the deep Mantle and the outer Core (microseism P and $PKPab$
 139 waves). In section 3, we estimate the temporal variations in the P_{dmc} amplitude and refute the
 140 associations to seismicity. In section 4, correlation analysis is used to unveil the spatiotemporal
 141 links of the P_{dmc} signal with the global oceanic wave climate and microseism sources. Last, we
 142 discuss the significance of this study in seismology, oceanography and climate science.

143 **2 Noise-derived P_{dmc} phase**

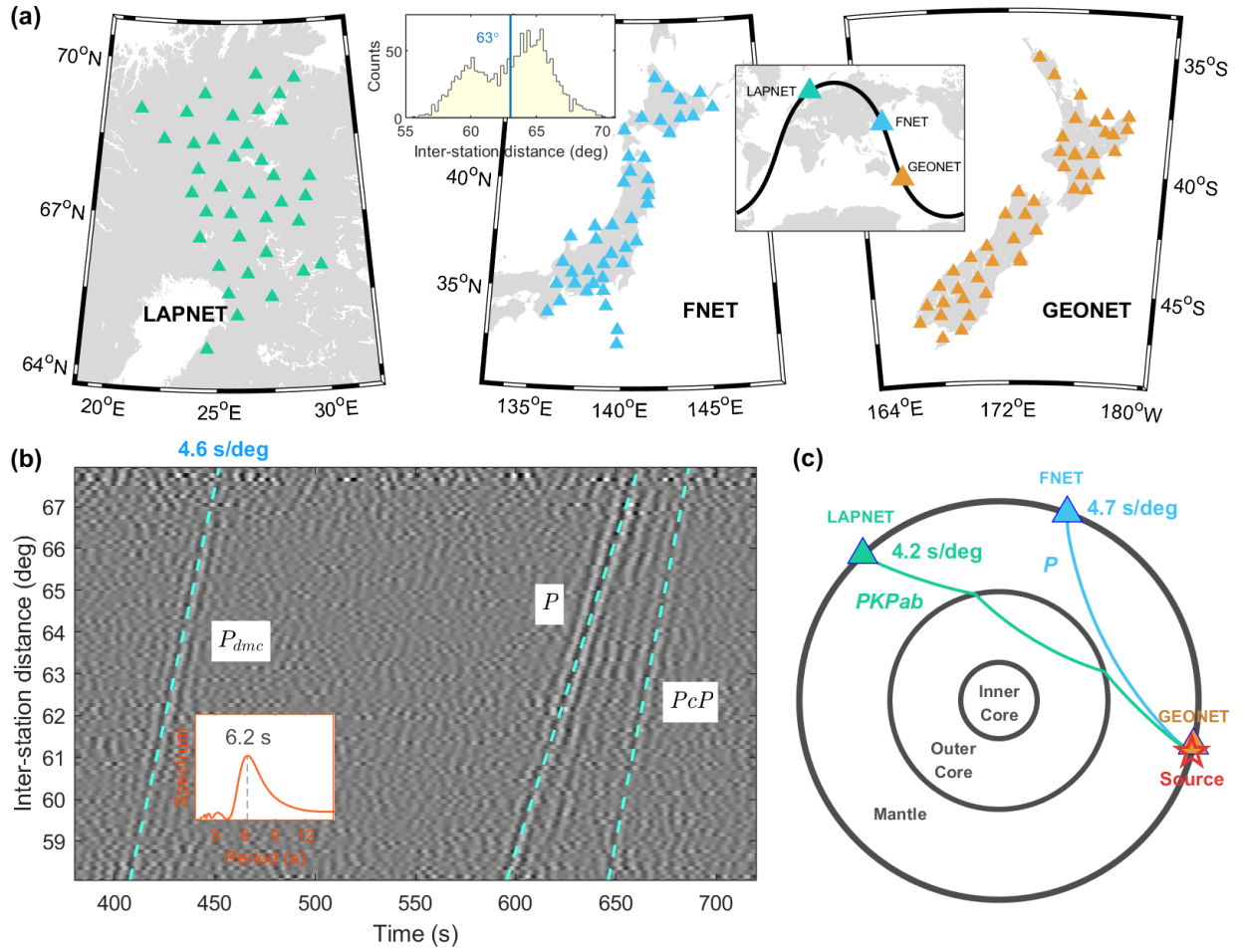
144 Li et al. (2020) correlated the seismic noise records from two regional seismic networks
 145 at teleseismic distance: the FNET array in Japan and the LAPNET array in Finland (Fig. 1a).
 146 From the vertical-vertical components of noise correlations between the FNET-LAPNET station
 147 pairs, they observed coherent spurious arrivals (the P_{dmc} phase named in the previous section)
 148 that emerged ~ 200 s earlier than the direct P waves (Fig. 1b). By estimating the respective
 149 slownesses of the interfering waves and their time delay, it is unveiled that a quasi-stationary
 150 phase interference between the teleseismic P waves at FNET and the $PKPab$ waves at LAPNET,
 151 emanating from noise sources in the ocean south of New Zealand (NZ), lead to the noise-derived
 152 P_{dmc} phase (Fig. 1c). The quasi-stationary phase condition refers to that the interfering waves
 153 have no common path or common slowness, but the stack of correlation functions over a range

154 of sources can still be constructive as an effect of finite frequency. This observation contrasts
155 with the strict stationary phase condition that has been employed by Phạm et al. (2018) to
156 explain the spurious body phases in the earthquake coda correlations. The strict condition implies
157 the existence of sources in the stationary-phase region, or say, the correlated waves have
158 common ray paths or common slownesses. Li et al. (2020) substantiates the explanation of quasi-
159 stationary phase for the observed P_{dmc} signals with numerical experiments based on ray theory
160 and based on spectral-element modeling, and highlighted the discrepancies between
161 (microseism) noise correlations and coda correlations.

162 The P_{dmc} phase has an apparent slowness of 4.6 s/deg, while the slownesses of the
163 interfering P and $PKPab$ waves are 4.7 s/deg and 4.2 s/deg, respectively. The dominant period of
164 the P_{dmc} phase is 6.2 s, typical for secondary microseisms. The observation of the P_{dmc} phase is
165 time-asymmetric (Fig. S1a). Its absence from the mirror side is ascribed to the faintness of the
166 corresponding source in the low-latitude Atlantic (Fig. S1b).

167 There are several advantages to investigate the links between noise-derived signals and
168 microseism sources with the P_{dmc} phase. First, the correlated P and $PKPab$ waves are both
169 prominent phases in the ballistic microseism wavefields. The P_{dmc} phase is easily observable
170 from noise correlations, even between some single station pairs and on some single days (Fig.
171 S2). Second, the isolation of P_{dmc} signals avoids potential bias caused by other prominent
172 signals. Third, the effective sources are confined in a limited, unique region (Fresnel zone). In
173 contrast, noise-derived surface waves have a broad Fresnel zone around the line across the
174 correlated stations, and noise-derived P waves can have multiple Fresnel zones (see fig. 5 of
175 Boué et al., 2014 for instance). The uniqueness of the effective source region can facilitate the
176 study on the correlation between the noise-derived signals and the effective sources. Fourth, the
177 correlated FNET and LAPNET networks are next to the northern Pacific and Atlantic,
178 respectively, while the effective source region locates in the southern Pacific. The northern
179 oceans have consistent seasonal variation pattern distinct from (reverse to) that of the southern
180 oceans (Stutzmann et al., 2009; Landès et al., 2010; Hillers et al., 2012). These geographical
181 configurations make the observations easier to interpret. Last, there happens to be a seismic array
182 (GEONET) in NZ next to the effective source region for the P_{dmc} phase. The seismic data from
183 GEONET provide extra support to our study.

184



185

186 Figure 1. (a) Three regional broadband seismic networks used in this study: left, the LAPNET
 187 array in Finland (38 stations); center, the FNET array in Japan (41 stations); right, the GEONET
 188 array in New Zealand (46 stations). The histogram inset shows the distribution of the separation
 189 distances between the 1558 FNET-LAPNET station pairs. The center-to-center distance is 63°
 190 between LAPNET and FNET, and 85° between FNET and GEONET. The global inset shows the
 191 geographical locations of the three networks that are aligned on a great circle (dark line). (b)
 192 FNET-LAPNET noise correlations that are filtered between 5 s and 10 s and stacked in 0.1° bins.
 193 The spectrum inset indicates that the P_{dmc} phase has a 6.2 s peak period. (c) Ray paths of the
 194 interfering waves that generate the P_{dmc} phase. The effective source region is close to GEONET.

195

196 3 Temporal variations

197 We extract the temporal variations of the P_{dmc} signals by beamforming the FNET-
 198 LAPNET noise correlations on a daily basis. The daily noise correlations are shifted and stacked
 199 by

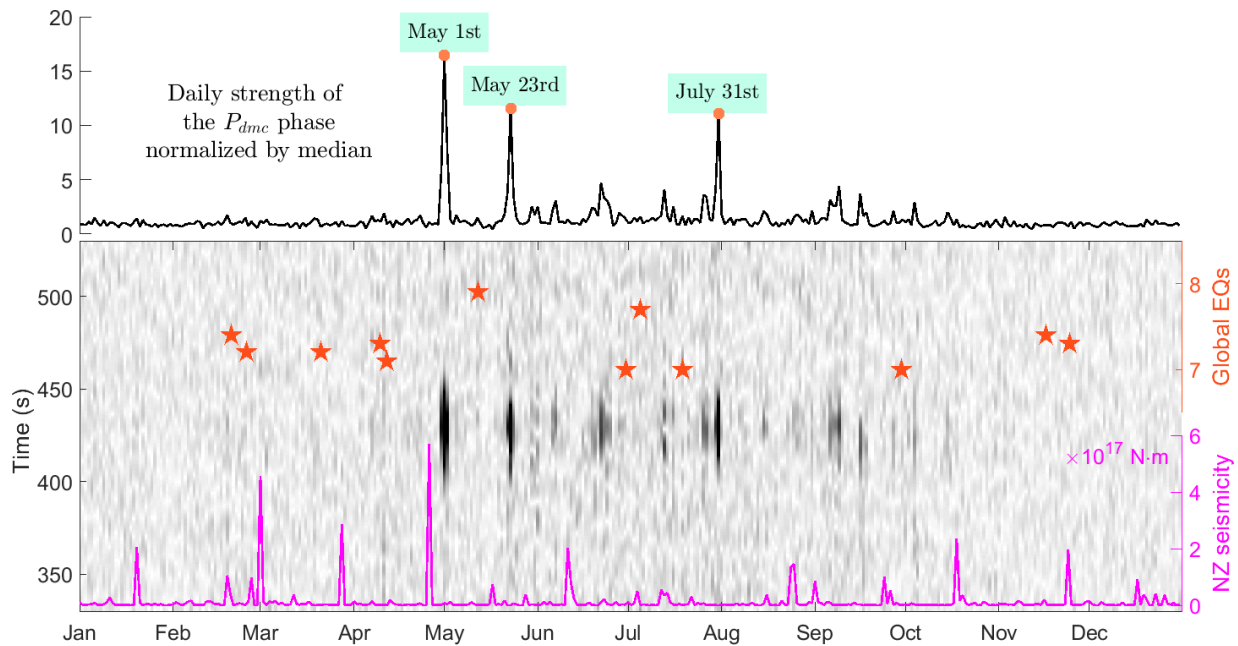
$$200 B(t) = \langle C_{ij}(t + (d_{ij} - d_0) \cdot p) \rangle, \quad (1)$$

201 with $\langle \cdot \rangle$ the mean operator, C_{ij} and d_{ij} the correlation function and the distance between the i th
 202 FNET station and the j th LAPNET station, d_0 the reference distance (63°), p the apparent

203 slowness of the P_{dmc} phase (4.6 s/deg), and t the time. The image in Fig. 2 shows the envelopes
 204 of the daily beams computed from the Hilbert transform of Eq. (1), with the daily P_{dmc} strength
 205 by averaging the envelope amplitudes plotted in the top panel. The strength of daily P_{dmc} signals
 206 varies strikingly, extremely strong on some single days (see the labeled dates in the P_{dmc} strength
 207 curve for examples), but indiscernible on most other days.

208 Considering that the region of effective source is tectonically active, one should
 209 investigate the plausible connection between the P_{dmc} signals and seismicity. From Fig. 2, it is
 210 obvious that P_{dmc} is decorrelated with the NZ seismicity. Also, it shows no relevance with global
 211 large earthquakes as has been observed for coda-derived core phases at periods of 20 to 50 s (Lin
 212 & Tsai, 2013; Boué et al., 2014). That again demonstrates the substantial difference between
 213 ambient noise correlations and earthquake coda correlations, as has been emphasized by Li et al.
 214 (2020). The P_{dmc} strength exhibits an obvious pattern of seasonal variation. The seasonal pattern
 215 does not favor a tectonic origin because of the lack of that in seismicity. Instead, an oceanic
 216 origin is more favored because of the well-documented fact that oceanic wave activities and
 217 microseism excitations show similar seasonal pattern: more powerful during the local winter
 218 (e.g., Stehly et al., 2006; Stutzmann et al., 2009; Landès et al., 2010; Hillers et al., 2012). Next,
 219 we analyze the correlations between P_{dmc} signals and oceanographic data at a global scale.

220



221

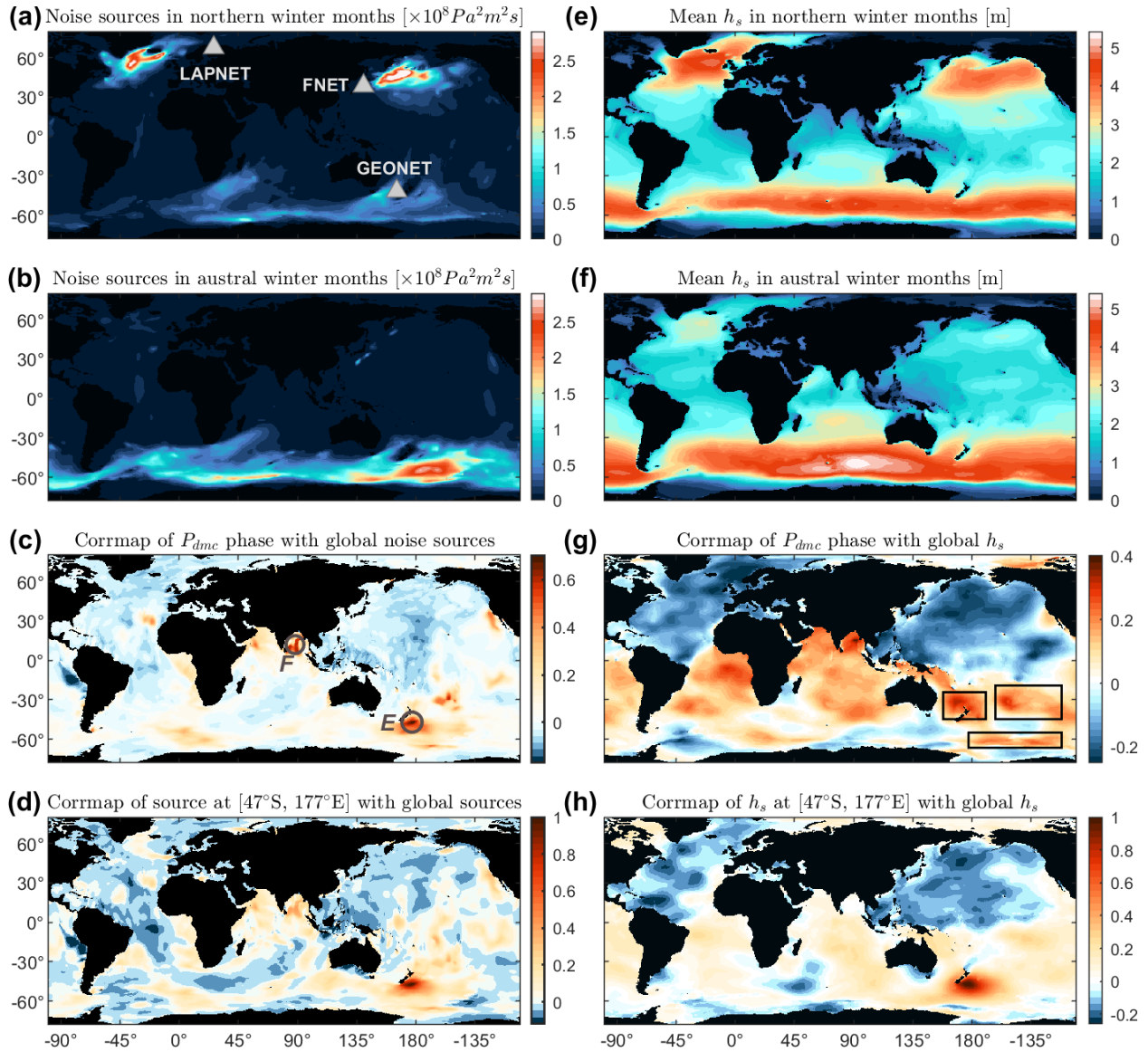
222 Figure 2. Temporal variations in the strength of daily P_{dmc} signals, in comparisons with the daily
 223 cumulative seismic moments in NZ (pink line at bottom; for earthquake magnitudes above 2.0 in
 224 GEONET catalogue) and global large earthquakes (stars; magnitudes above 7.0 in USGS
 225 catalogue). The background image is composed of columns of daily envelopes of beamed FNET-
 226 LAPNET noise correlations. Darker color represents larger amplitude. The curve on the top
 227 shows the daily P_{dmc} strength derived from the daily envelopes. Dates of the three largest peaks
 228 are labeled.

229 4 Correlation analysis

230 The sea state is composed of ocean waves at various frequencies and propagation
 231 directions. The nonlinear interaction between nearly equal-frequency ocean waves traveling in
 232 nearly opposite directions is equivalent to a vertical random pressure applied to the ocean surface
 233 (Longuet-Higgins, 1950; Hasselmann, 1963), so that microseisms are generated. Figure 3(a)
 234 shows a global map of average Power Spectral Density (PSD) of the equivalent surface pressure
 235 for a seismic period of 6.2 s, during the northern winter months of 2008. The most energetic
 236 microseism excitations occur in the northern Atlantic south of Greenland and Iceland (near
 237 LAPNET), and in the northern Pacific between Japan and Alaska (near FNET). Figure 3(b)
 238 shows the map for the austral winter months, with the strongest excitations occurring between
 239 NZ and Antarctic (near GEONET). The seasonal pattern of oceanic microseism excitations
 240 results from the same pattern of global wave climate (Figs 3e-f). The seasonal pattern of the P_{dmc}
 241 strength agrees with that of the microseism excitation and wave climate in the effective source
 242 region south of NZ.

243 We compute the correlation coefficient (denoted as r) between the P_{dmc} strength and the
 244 source PSDs at each grid point, and thereby obtain a global correlation map (Fig. 3c). The largest
 245 r value for P_{dmc} and source PSD arises at $[47^\circ\text{S}, 177^\circ\text{E}]$ in the effective source region (E in Fig.
 246 3c). The corresponding time series of daily source PSDs is plotted in Fig. 4, in parallel with the
 247 P_{dmc} strength. Large peaks in the P_{dmc} series have good correspondence with large peaks in the
 248 source PSD series. From Fig. 3(c), one can observe a broad region of positive r values (red
 249 colors; roughly, south Atlantic, south Pacific, and Indian ocean). However, the positive
 250 correlation does not imply a causality between the P_{dmc} phase and the sources outside the
 251 effective region E . We ascribe the apparent positive correlation to the spatial correlation of the
 252 time-varying microseism excitation. As shown in Fig. 3(d), the source at $[47^\circ\text{S}, 177^\circ\text{E}]$ in region
 253 E exhibits a similar pattern of apparent correlations with global sources as in Fig. 3(c). It has
 254 been known that the microseism excitations at varying locations are independent (Hasselmann,
 255 1963). However, we note that the independence refers only to the phase information. The time
 256 variations of microseism source power are spatially associated. That is not surprising since the
 257 interacting ocean waves that excite microseisms could be driven by the same storms and swells
 258 can propagate freely over thousands of kilometers away (Ardhuin et al., 2009). We also notice
 259 there are high- r regions that may not be fully explained by the spatial association. These regions
 260 are characterized by low intensity of microseism excitations in Figs 3(a-b). A striking example is
 261 around $[12^\circ\text{N}, 88^\circ\text{E}]$ in the Bay of Bengal (F in Fig. 3c). From Fig. 4, it can be seen that the
 262 source PSD series for $[12^\circ\text{N}, 88^\circ\text{E}]$ is dominated by a single peak around May 1st, coincident
 263 with the largest P_{dmc} peak. This coincidence leads to a fake high correlation. Figures 3(g-h) show
 264 the correlation maps for h_s , which will be discussed later.

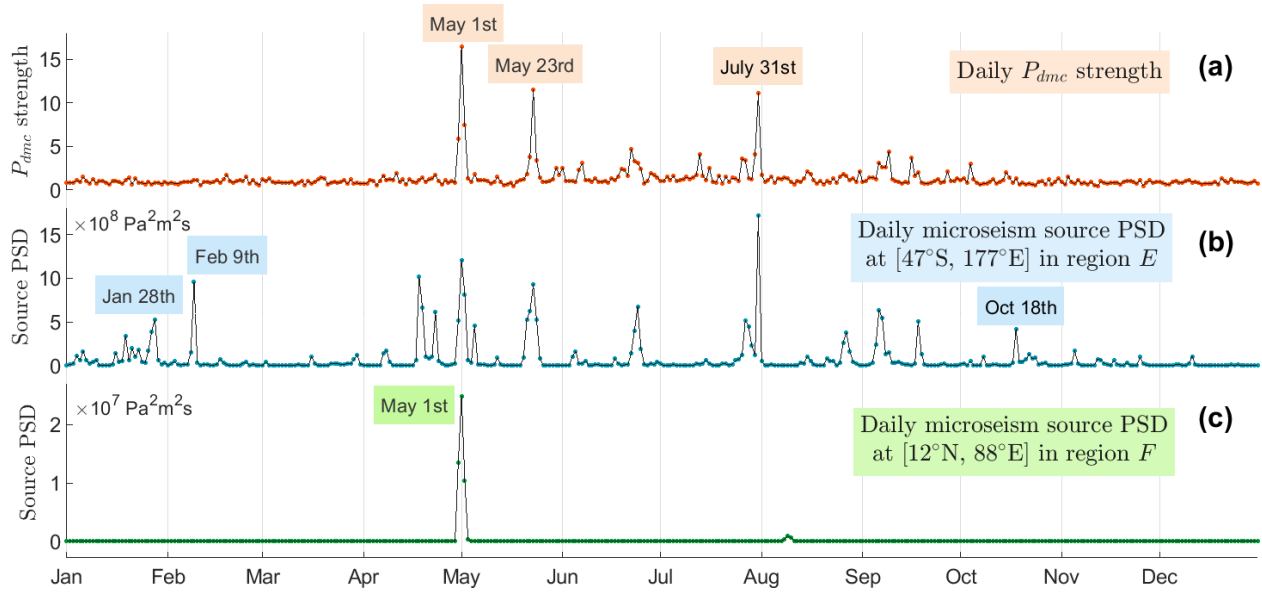
265



266

267 Figure 3. (a) Global map of average PSD of oceanic microseism sources in 2008 northern winter
 268 months (Jan. to Mar. and Oct. to Dec.), for a seismic period of 6.2 s. (b) Similar to (a) but for
 269 2008 austral winter months (Apr. to Sep.). (c) Correlation map (corrmap) for the P_{dmc} strength
 270 and global microseism noise sources. Circles mark two regions with highest correlation
 271 coefficients: *E*, effective source region surrounding $[47^\circ S, 177^\circ E]$ south of NZ; *F*, fake highly-
 272 correlated region surrounding $[12^\circ N, 88^\circ E]$ in the Bay of Bengal. (d) Correlation map for the
 273 source at $[47^\circ S, 177^\circ E]$ and global sources. (e) Mean significant wave height (h_s ; four times the
 274 square root of the zeroth-order moment of ocean-wave frequency spectrum) in northern winter
 275 months. (f) Similar to (e) but for austral winter months. (g) Correlation map for the P_{dmc} strength
 276 and global wave heights. (h) Correlation map for wave heights at $[47^\circ S, 177^\circ E]$ and global wave
 277 heights. The oceanographical hindcast data are provided by the IOWAGA products (Rascle &
 278 Ardhuin, 2013).

279



280

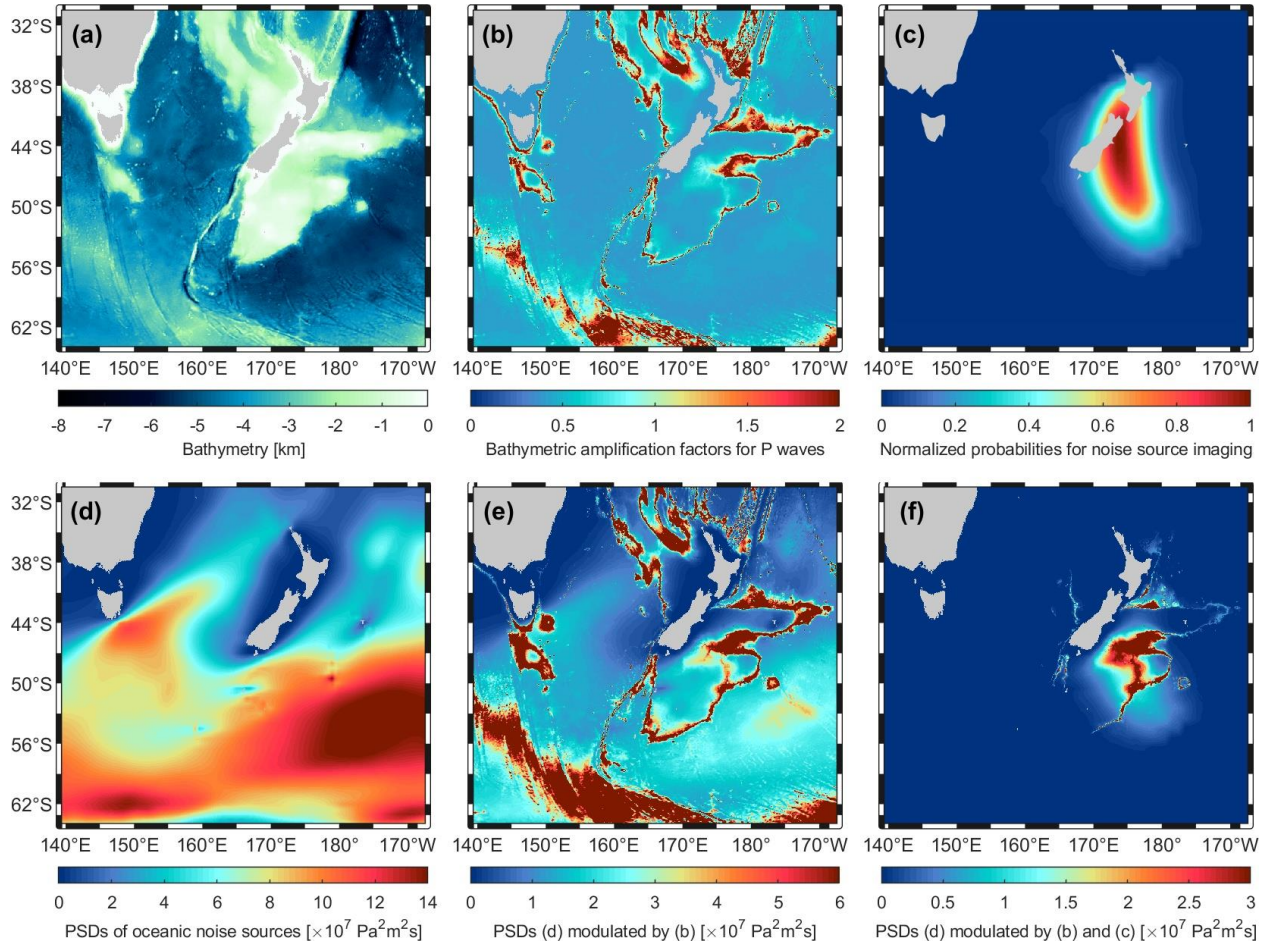
281 Figure 4. True correlation ($r = 0.73$) between (a) the P_{dmc} strength from Fig. 2 and (b) the power of source at $[47^\circ\text{S}, 177^\circ\text{E}]$ in the effective source region (E in Fig. 3c), and false correlation ($r =$
 282 0.71) between P_{dmc} and (c) the power of source at $[12^\circ\text{N}, 88^\circ\text{E}]$ in the Bay of Bengal (F in Fig.
 283 3c).
 284

285

286 As shown in Fig. 4, prominent peaks in the P_{dmc} series have correspondence in the source
 287 PSD series for the effective source at $[47^\circ\text{S}, 177^\circ\text{E}]$. However, there are some peaks in the latter
 288 without correspondence in the former (see the labeled dates in Fig. 4b for examples). Note that
 289 here the P_{dmc} strength is compared to the microseism source PSD at single point in Fig. 4,
 290 whereas the effective sources spread over a region. One needs to verify if the peak disparities
 291 observed from Figs 4(a-b) can be ascribed to the neglect of the spreading of the effective source
 292 region. To evaluate an overall microseism excitation in the effective source region, the
 293 bathymetric effect on P -wave excitation should be considered (in the previous analysis for single
 294 point locations, the consideration of bathymetric effect is unnecessary because a scaling over the
 295 source PSD series does not change the value of the correlation coefficient between P_{dmc} and
 296 source PSD). Using the equations proposed by Gualtieri et al. (2014) and the bathymetry around
 297 NZ (Fig. 5a), we compute the bathymetric amplification factors for P waves at a period of 6.2 s
 298 (Fig. 5b; see Fig. S3 for comparisons between the factors calculated following Longuet-Higgins,
 299 1950 and Gualtieri et al., 2014). The factors vary largely over locations. Also, note that the P_{dmc}
 300 phase has different sensitivity to the sources in the effective region, or say, the sources make
 301 varying contributions to the P_{dmc} signal. The power of sources should be weighted in the
 302 averaging. We obtain the weights by back-projecting the beam power of noise correlations onto a
 303 global grid (Fig. 5c; see Supplementary for technical details). Figure 5(d) shows the map of
 304 annually averaged source PSDs surrounding NZ and Fig. 5(e) shows the map after the
 305 modulation of the bathymetric amplification factors in Fig. 5(b). The spatial patterns are altered
 306 significantly, indicating the importance to account for the bathymetric effect. The final source
 307 imaging that has been weighted by Fig. 5(c), is plotted in Fig. 5(f), which agrees well with the
 308 effective source region E determined from the correlation map in Fig. 3(c). Replacing the annual
 309 PSD map in Fig. 5(d) with daily PSD maps, we obtain maps like Fig. 5(f) for each date.

310 Averaging over the map leads to the time series of daily intensity in the effective source region
 311 (labeled as effective source intensity in Fig. 6). The new series has almost the same peaks as the
 312 series for [47°S, 177°E] in Fig. 4(b), suggesting that the observed peak disparities are caused by
 313 other reasons. Next, we investigate if the disparities are caused by errors in the simulation of
 314 hindcast data or if there are other physical explanations.

315



316

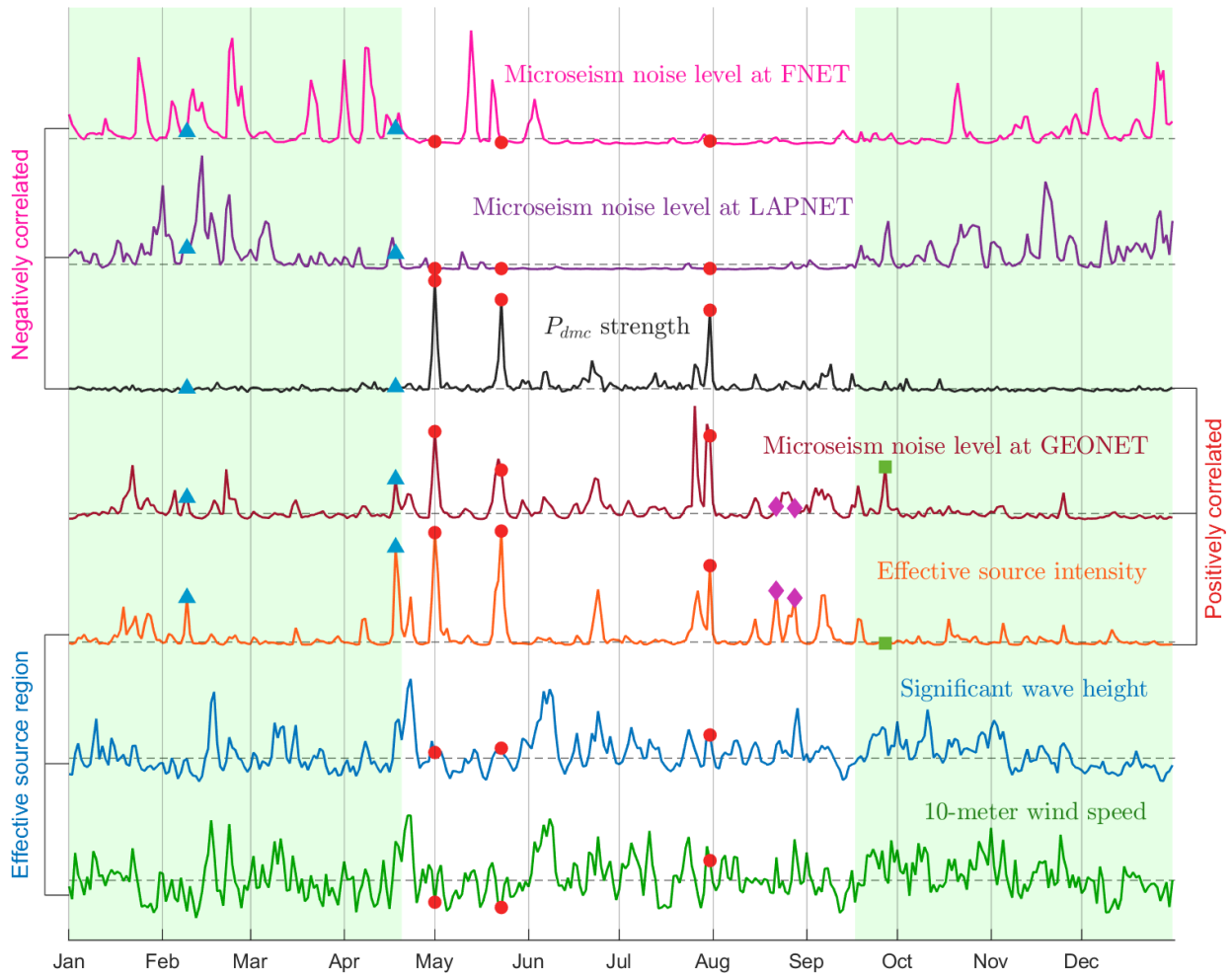
317 Figure 5. (a) Bathymetry around NZ. (b) Bathymetric amplification factors for P -type waves. (c)
 318 Imaging of effective sources obtained from the back-projection of the FNET-LAPNET noise
 319 correlations. (d) Annual average of source PSDs in 2008. (e) Source PSDs in (d) modulated by
 320 the factors in (b). (f) Source PSDs in (e) further modulated by the weights in (c).

321

322 The microseism source PSD data are simulated from the hindcast data of ocean wave
 323 directional spectra base on the excitation theory of Longuet-Higgins (1950) and Hasselmann
 324 (1963), which have no constrains from seismological observations. One should consider the
 325 accuracy of the simulation: can we ascribe the peak disparities in Fig. 4 to the simulation error or
 326 not? The seismic noise records from the GEONET array adjacent to the effective source region
 327 provide the opportunity to validate the simulation. To obtain the daily microseism noise levels at
 328 GEONET, we apply the Hampel filter, a variant of the classic median filter, to the continuous
 329 seismograms to discard earthquakes and anomalous impulses. The filter replaces outliers with

330 the medians of the outliers' neighbors and retains the normal samples. Technical details are
 331 provided in section S4 of the Supplementary. The resultant GEONET noise level exhibits a good
 332 correlation with the effective source intensity ($r = 0.7$). We thus deem that the numerical
 333 simulations are statistically reliable. When the effective source intensity is high, the GEONET
 334 noise level should also be high (see the peaks marked by dots in Fig. 6 for examples). However,
 335 due to the great spatiotemporal variability of noise sources in the effective region and the
 336 complexity of seismic waves propagating from ocean to land (Ying et al., 2014; Gualtieri et al.,
 337 2015), a larger peak in the source intensity series does not necessarily imply a larger peak in the
 338 noise level time series (e.g., see diamonds in Fig. 6 for examples). We also emphasize that a high
 339 GEONET noise level does not need to always have a correspondence in the source intensity (see
 340 squares in Fig. 6 for example), because the GEONET stations record microseisms emanating
 341 from noise sources all around, not only from the effective source region.

342



343

344 Figure 6. Temporal variations of daily P_{dmc} strength, microseism noise levels at three networks,
 345 and average wind speeds, wave heights and microseism excitations in the effective source
 346 region. The curves are normalized by their own maximums. Dashed horizontal lines denote their
 347 respective medians. Symbols mark some dates cited in the main text. When computing the
 348 effective source intensity, the bathymetric factors in Fig. 5(b) and weights in Fig. 5(c) are used.
 349 When computing the average wind speeds and wave heights, weights in Fig. 5(c) are used.

350

351 The above analysis explains the observed disparities between the P_{dmc} strength and the
 352 effective source intensity. From Fig.6, one can see that the disparities primarily emerge in the
 353 shaded period when dominant microseism sources shift to the north hemisphere. The shading
 354 roughly separates the northern winter from the austral winter. The correlation between P_{dmc}
 355 strength and effective source intensity is low in the shaded period ($r = 0.16$), in contrast to the
 356 high correlation during the unshaded period ($r = 0.74$). Large P_{dmc} peaks always emerge on dates
 357 during the austral winter when the effective source intensity is much higher than its median, and
 358 meanwhile, noise levels at FNET and LAPNET are below their respective medians (see dots in
 359 Fig. 6 for examples). The seasonal variations of oceanic sources in the south hemisphere are less
 360 strong than in the north hemisphere (Fig. 3). On some dates (see triangles in Fig. 6 for
 361 examples), the effective source intensity can be considerable, but relevant P_{dmc} peaks are still
 362 missing. We notice that the corresponding microseism levels at FNET and LAPNET are
 363 obviously above their medians. Intensive ocean activities and microseism excitations in the north
 364 Pacific and Atlantic, lead to increased microseism noise levels at FNET and LAPNET. The P_{dmc}
 365 strength is anti-correlated with microseism noise levels at FNET ($r = -0.12$) and LAPNET ($r = -$
 366 0.18). We hereby conjecture that the microseism energy from the distant effective source region
 367 is dwarfed by the energetic microseisms excited by oceanic sources closer to the correlated
 368 FNET and LAPNET arrays, and consequently, P_{dmc} signals are overwhelmed by the background
 369 noise in the FNET-LAPNET cross-correlations.

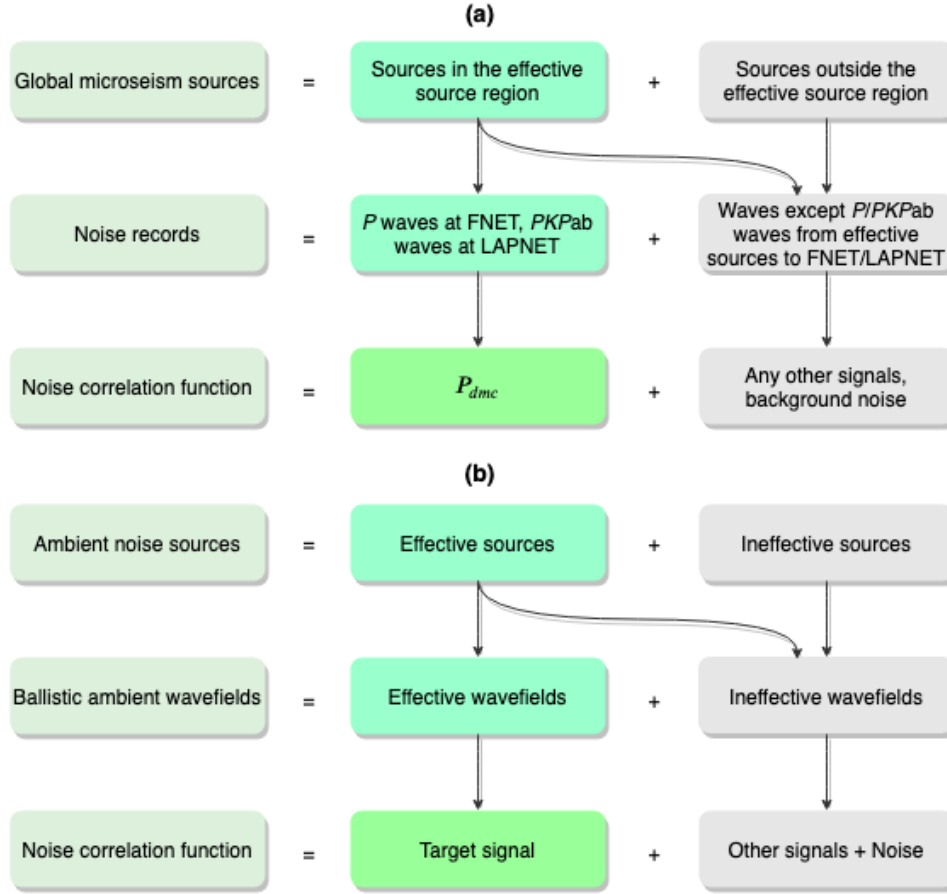
370 5 Discussions and conclusions

371 In this study, we analyzed the spatiotemporal correlations between noise-derived P_{dmc}
 372 signals and global oceanic microseism sources. In our case, the correlated seismic networks are
 373 located in the north hemisphere, while the effective source region is in the south hemisphere.
 374 Ideally, we expect a correlation map with the following features: positive correlation with
 375 sources in the effective region, and negative or insignificant correlations with other inefficient
 376 sources. Positive correlation indicates a contribution to the construction of P_{dmc} signal from noise
 377 correlations, negative correlation implies an adverse impact, and insignificant correlation
 378 (decorrelation) means a negligible effect on the signal construction. However, we obtained a
 379 correlation map roughly showing that, the P_{dmc} signal is correlated with the southern sources and
 380 anti-correlated with the northern sources. The correlation with southern sources outside the
 381 effective region can be interpreted with the spatiotemporal correlation of the power of the
 382 microseism sources in the southern oceans, due to the large span of ocean storms and the long-
 383 range propagation of swells. The anti-correlation with the northern sources, can partly be
 384 explained by the reverse seasonal patterns of oceanic microseism excitations in the south and
 385 north hemispheres. Another important reason is that compared to the remote effective sources in
 386 the south hemisphere, the northern sources closer to the correlated stations have larger impacts
 387 on the microseism noise levels at stations. Strong energy flux from the northern sources

388 outshines the microseism energy coming from the distant effective sources. That deteriorates the
 389 construction of the P_{dmc} phase. The noise-derived P_{dmc} signals are primarily observable in the
 390 austral winter. That can be, on one hand, attributed to the stronger effective source excitation
 391 during that period, and on the other hand, to the relative tranquility in the north oceans.

392 In Fig. 7, we summarize the classification of noise sources, the decomposition of
 393 wavefields, and the associations to the constituents of the inter-receiver noise correlation
 394 function. The diagram of Fig. 7(a) explains the relationships using the case study of the P_{dmc}
 395 phase discussed above. We generalize Fig. 7(a) to the derivation of an arbitrary signal (referred
 396 to as the target signal for convenience) from ambient noise wavefields (Fig. 7b). The noise
 397 correlation function is composed of the target signal, any other signals and background noise. A
 398 source or a wave is called effective if it contributes to the construction of the target signal from
 399 noise correlations. Otherwise, it is called ineffective. The construction of the target signal is
 400 exclusively ascribed to the interference between the effective waves. Stronger effective sources
 401 (relative to ineffective sources) imply more effective waves in the total wavefield, and thereby, a
 402 better quality for the noise-derived target signal. Note that not all waves emanating from the
 403 effective sources, but only those following specific ray paths, are effective. There might be
 404 multiple pairs of seismic phases that could contribute to the construction of the target signal.
 405 However, their relative strength matters. As for the case of the P_{dmc} phase, the effective waves
 406 are P and $PKPab$, which are both prominent phases in the ballistic wavefield. Li et al. (2020)
 407 showed that the PcP - $PKPab$ correlation and the PcS - $PcPPcP$ correlation, could also lead to a
 408 signal at around the P_{dmc} emerging time. However, the PcP , PcS , and $PcPPcP$ waves are weak
 409 phases in the ballistic wavefield, and thereby have minor contributions to the P_{dmc} signals. We
 410 emphasize that the sketch in Fig. 7(b) is only suitable for the ambient noise wavefields that are
 411 dominated by ballistic waves.

412



413

414 Figure 7. (a) Sketch explanation for the relationships between microseism noise sources and the
 415 noise-derived P_{dmc} signal. (b) Generalization of diagram (a) for an arbitrary signal derived from
 416 ambient noise wavefields that are dominated by ballistic waves.

417

418 The effective source region E for the P_{dmc} phase is successfully identified from the
 419 correlation map in Fig. 3(c). It is consistent with that determined from the seismological back-
 420 projection in Fig. 5(c). The correlation map provides an easy way to identify the effective
 421 sources for noise-derived seismic signals. The double-array back-projection is superior to the
 422 classic single-array back-projection in reducing the ambiguity in the detection and location of
 423 microseism events. A catalogue of microseism events would be promising in teleseismic body-
 424 wave tomography (Zhang et al., 2010; Boué et al., 2013; Nishida & Takagi, 2016). The good
 425 consistency of the temporal variations in the P_{dmc} strength, the effective source intensity and the
 426 NZ microseism noise level (Fig. 6), provides extra supports to the analysis of the P_{dmc}
 427 observations and the quasi-stationary phase arguments proposed by Li et al. (2020). It also gives
 428 credits to the validity of the numerical modeling of oceanic microseism sources by Arduin et al.
 429 (2011) and Rasclé & Arduin (2013).

430 In the P_{dmc} - h_s correlation map in Fig. 3(g), the largest r values do not fall in region E as in
 431 Fig. 3(c), but in surrounding regions with moderate to high ocean wave activities (the bounded
 432 areas). We speculate that these regions could be the birthplaces of the colliding swells that
 433 generate the secondary microseisms in region E , or the ocean waves in these regions are driven

434 by the same storms as the colliding waves in region E (see the spatial links of h_s from Fig. 3h and
435 supplementary movie S1). From Fig. 6, one can observe a high correlation between wind speed
436 and wave height in region E ($r = 0.74$). It indicates that the ocean waves in region E are likely
437 dominated by the waves forced by local winds. The correlation between wave height and
438 microseism excitation is low ($r = 0.25$), implying a dominant role of the freely propagating
439 swells in exciting the microseisms. Extreme sea state does not guarantee strong microseism
440 excitation. That is not surprising according to the microseism excitation theory (Hasselmann,
441 1963; Longuet-Higgins, 1950): the excitation is proportional to the product of the heights of the
442 colliding equal-frequency ocean waves. In lack of equal-frequency waves coming from opposite
443 directions, even extreme wave climate cannot incite strong secondary microseisms. In contrast,
444 for large peaks in the microseism excitation, the corresponding wave heights are generally
445 moderate (e.g., on May 1st and 23rd). On these two dates, the low wind speeds but moderate
446 wave heights in region E suggest that the ocean waves are dominantly the freely travelling swells
447 from elsewhere, as also illustrated in the supplementary movie S1. Oppositely propagating equal-
448 frequency swells collide with each other and incite strong microseisms. Obrebski et al. (2012)
449 reported similar observations in the eastern Pacific. There are also few examples that wind waves
450 can play a role in the excitation of microseisms, for instance, around July 31st when the local
451 winds, wave height, and microseism excitations are all strong.

452 We have described above the implications of this study in seismology and in
453 understanding the process of microseism excitation. Now, we discuss the significance in
454 oceanography and climate science. Well-documented historical ocean storms and wave climate
455 are valuable for improving our understanding about climate change and global warming (Ebeling
456 2012). However, modern satellite observations of ocean waves and storms have a history of
457 merely decades. Microseisms are induced by storm-driven ocean waves (Ardhuin et al., 2015;
458 Hasselmann, 1963; Longuet-Higgins, 1950). The records of microseisms contain the imprint of
459 climate (Aster et al., 2010; Stutzmann et al., 2009). Instrumental observation of microseisms has
460 an over-century history, much earlier than the modern observations of ocean waves and storms.
461 It has been a long-lasting effort for the seismological community to digitalize the historical
462 analog seismograms (Bogiatzis & Ishii, 2016; Lecocq et al., 2020). Researchers expect that past
463 seismic records can be used to recover undocumented historical ocean storms and wave climate
464 (Ebeling 2012; Lecocq et al., 2020). The correlation analysis in this study confirms that it is
465 practicable to detect remote microseism events (burst of microseism energy) with land
466 observation of microseisms. The event detection could be effective when there are no strong
467 sources near the station, otherwise it could be missed. It suggests that stations at low latitudes
468 where wave climate and microseism excitation are relatively mild, or inland stations far from
469 oceans, should have better performance in remote detection. Energetic microseism excitation
470 does not always need extremal in situ wave heights, and extremal wave height does not
471 necessarily produce powerful microseisms. These imply that secondary microseism events are
472 not a perfect proxy for the extremal in situ wave climate. However, it does not mean the long-
473 lasting attempt to monitor remote sea state and ocean storms with land observation of secondary
474 microseisms is futile. The detection of a microseism event could affirm the existence of the
475 causative storms that generated the ocean waves propagating to the location of the microseism
476 event, despite the storms could be distant from the events.

477

478 **Acknowledgments and data**

479 The seismic data of FNET and LAPNET were provided by the National Research
 480 Institute for Earth Science and Disaster Resilience (<http://www.fnet.bosai.go.jp/>; last access:
 481 June 2018) and the Réseau Sismologique & Géodésique Français (<http://www.resif.fr/>; last
 482 access: June 2018), respectively. The seismic data of GEONET and the earthquake catalogue of
 483 New Zealand were provided by the GEONET Data Center (<https://www.geonet.org.nz/>; last
 484 access: June 2018). The global earthquake catalogue was provided by the U.S. Geological
 485 Survey (<https://earthquake.usgs.gov/>; last access: June 2018). The wind hindcast data were
 486 provided by the European Centre for Medium-Range Weather Forecasts
 487 (<https://www.ecmwf.int/>; last access: June 2018). The hindcast data of wave heights and
 488 microseism source PSDs were provided by the IOWAGA products (Rascle & Arduin, 2013).
 489 The bathymetry data were extracted from ETOPO1 Global Relief Model (Amante & Eakins,
 490 2009). The computations were performed mainly on the ISTERre cluster. This work was
 491 supported by Labex OSUG@2020 (Investissements d'avenir-ANR10LABX56) and the Simone
 492 and Cino del Duca Foundation, Institut de France. We acknowledge the support from the
 493 European Research Council (ERC) under the European Union's Horizon 2020 research and
 494 innovation program (grant agreement No 742335, F-IMAGE).

495

496 **References**

- 497 Amante, C., & Eakins, B. W. (2009). *ETOPO1 1 Arc-Minute Global Relief Model: Procedures,*
 498 *Data Sources and Analysis. NOAA Technical Memorandum NESDIS NGDC-24.*
 499 <https://doi.org/10.7289/V5C8276M>
- 500 Arduin, F., Chapron, B., & Collard, F. (2009). Observation of swell dissipation across oceans.
 501 *Geophysical Research Letters*, 36(6), L06607. <https://doi.org/10.1029/2008GL037030>
- 502 Arduin, F., Stutzmann, E., Schimmel, M., & Mangeney, A. (2011). Ocean wave sources of
 503 seismic noise. *Journal of Geophysical Research: Oceans*, 116(9), 1–21.
 504 <https://doi.org/10.1029/2011JC006952>
- 505 Arduin, F., Gualtieri, L., & Stutzmann, E. (2015). How ocean waves rock the Earth: Two
 506 mechanisms explain microseisms with periods 3 to 300s. *Geophysical Research Letters*,
 507 42(3), 765–772. <https://doi.org/10.1002/2014GL062782>
- 508 Aster, R. C., McNamara, D. E., & Bromirski, P. D. (2010). Global trends in extremal microseism
 509 intensity. *Geophysical Research Letters*, 37(14), 1–5.
 510 <https://doi.org/10.1029/2010GL043472>
- 511 Bernard, P. (1990). Historical sketch of microseisms from past to future. *Physics of the Earth*
 512 *and Planetary Interiors*, 63(3–4), 145–150. [https://doi.org/10.1016/0031-9201\(90\)90013-](https://doi.org/10.1016/0031-9201(90)90013-N)
 513 N
- 514 Bogiatzis, P., & Ishii, M. (2016). DigitSeis: A New Digitization Software for Analog
 515 Seismograms. *Seismological Research Letters*, 87(3), 726–736.
 516 <https://doi.org/10.1785/0220150246>

- 517 Boué, P., Poli, P., Campillo, M., Pedersen, H., Briand, X., & Roux, P. (2013). Teleseismic
518 correlations of ambient seismic noise for deep global imaging of the Earth. *Geophysical*
519 *Journal International*, 194(2), 844–848. <https://doi.org/10.1093/gji/ggt160>
- 520 Boué, P., Poli, P., Campillo, M., & Roux, P. (2014). Reverberations, coda waves and ambient
521 noise: Correlations at the global scale and retrieval of the deep phases. *Earth and*
522 *Planetary Science Letters*, 391, 137–145. <https://doi.org/10.1016/j.epsl.2014.01.047>
- 523 Campillo, M., & Paul, A. (2003). Long-Range Correlations in the Diffuse Seismic Coda.
524 *Science*, 299(5606), 547–549. <https://doi.org/10.1126/science.1078551>
- 525 Dewey, J., & Byerly, P. (1969). The early history of Seismometry (to 1900). *Bulletin of the*
526 *Seismological Society of America*, 59(1), 183–227.
- 527 Ebeling, C. W. (2012). Inferring Ocean Storm Characteristics from Ambient Seismic Noise. In
528 R. Dmowska (Ed.), *Advances in Geophysics* (Vol. 53, pp. 1–33). Elsevier.
529 <https://doi.org/10.1016/B978-0-12-380938-4.00001-X>
- 530 Euler, G. G. G., Wiens, D. D. A., & Nyblade, A. A. (2014). Evidence for bathymetric control on
531 the distribution of body wave microseism sources from temporary seismic arrays in
532 Africa. *Geophysical Journal International*, 197(3), 1869–1883.
533 <https://doi.org/10.1093/gji/ggu105>
- 534 Gerstoft, P., Shearer, P. M., Harmon, N., & Zhang, J. (2008). Global P, PP, and PKP wave
535 microseisms observed from distant storms. *Geophysical Research Letters*, 35(23), 4–9.
536 <https://doi.org/10.1029/2008GL036111>
- 537 Gualtieri, L., Stutzmann, E., Farra, V., Capdeville, Y., Schimmel, M., Arduin, F., & Morelli, A.
538 (2014). Modelling the ocean site effect on seismic noise body waves. *Geophysical*
539 *Journal International*, 197(2), 1096–1106. <https://doi.org/10.1093/gji/ggu042>
- 540 Gualtieri, L., Stutzmann, E., Capdeville, Y., Farra, V., Mangeney, A., & Morelli, A. (2015). On
541 the shaping factors of the secondary microseismic wavefield. *Journal of Geophysical*
542 *Research B: Solid Earth*, 120(9), 6241–6262. <https://doi.org/10.1029/2000GC000119>
- 543 Harrison, E. P. (1924). Microseisms and Storm Forecasts. *Nature*, 114(2870), 645–645.
544 <https://doi.org/10.1038/114645b0>
- 545 Hasselmann, K. (1963). A statistical analysis of the generation of microseisms. *Reviews of*
546 *Geophysics*, 1(2), 177–210. <https://doi.org/10.1029/RG001i002p00177>
- 547 Hillers, G., Graham, N., Campillo, M., Kedar, S., Landès, M., & Shapiro, N. (2012). Global
548 oceanic microseism sources as seen by seismic arrays and predicted by wave action
549 models. *Geochemistry, Geophysics, Geosystems*, 13(1), Q01021.
550 <https://doi.org/10.1029/2011GC003875>
- 551 Kedar, S., Longuet-Higgins, M., Webb, F., Graham, N., Clayton, R., & Jones, C. (2008). The
552 origin of deep ocean microseisms in the North Atlantic Ocean. *Proceedings of the Royal*
553 *Society A: Mathematical, Physical and Engineering Sciences*, 464(2091), 777–793.
554 <https://doi.org/10.1098/rspa.2007.0277>
- 555 Landès, M., Hubans, F., Shapiro, N. M., Paul, A., & Campillo, M. (2010). Origin of deep ocean
556 microseisms by using teleseismic body waves. *Journal of Geophysical Research: Solid*
557 *Earth*, 115(5), 1–14. <https://doi.org/10.1029/2009JB006918>

- 558 Lecocq, T., Arduin, F., Collin, F., & Camelbeeck, T. (2020). On the Extraction of Microseismic
559 Ground Motion from Analog Seismograms for the Validation of Ocean-Climate Models.
560 *Seismological Research Letters*. <https://doi.org/10.1785/0220190276>
- 561 Li, L., Boué, P., & Campillo, M. (2020). Observation and explanation of spurious seismic signals
562 emerging in teleseismic noise correlations. *Solid Earth*, *11*(1), 173–184.
563 <https://doi.org/10.5194/se-11-173-2020>
- 564 Lin, F. C., & Tsai, V. C. (2013). Seismic interferometry with antipodal station pairs. *Geophysical*
565 *Research Letters*, *40*(17), 4609–4613. <https://doi.org/10.1002/grl.50907>
- 566 Lin, F. C., Tsai, V. C., Schmandt, B., Duputel, Z., & Zhan, Z. (2013). Extracting seismic core
567 phases with array interferometry. *Geophysical Research Letters*, *40*(6), 1049–1053.
568 <https://doi.org/10.1002/grl.50237>
- 569 Liu, Q., Koper, K. D., Burlacu, R., Ni, S., Wang, F., Zou, C., et al. (2016). Source locations of
570 teleseismic P, SV, and SH waves observed in microseisms recorded by a large aperture
571 seismic array in China. *Earth and Planetary Science Letters*, *449*, 39–47.
572 <https://doi.org/10.1016/j.epsl.2016.05.035>
- 573 Longuet-Higgins, M. S. (1950). A Theory of the Origin of Microseisms. *Philosophical*
574 *Transactions of the Royal Society A: Mathematical, Physical and Engineering Sciences*,
575 *243*(857), 1–35. <https://doi.org/10.1098/rsta.1950.0012>
- 576 Meschede, M., Stutzmann, E., Farra, V., Schimmel, M., & Arduin, F. (2017). The Effect of
577 Water Column Resonance on the Spectra of Secondary Microseism P Waves. *Journal of*
578 *Geophysical Research: Solid Earth*, *122*(10), 8121–8142.
579 <https://doi.org/10.1002/2017JB014014>
- 580 Meschede, M., Stutzmann, E., & Schimmel, M. (2018). Blind source separation of temporally
581 independent microseisms. *Geophysical Journal International*, *216*(2), 1260–1275.
582 <https://doi.org/10.1093/gji/ggy437>
- 583 Nishida, K. (2013). Global propagation of body waves revealed by cross-correlation analysis of
584 seismic hum. *Geophysical Research Letters*, *40*(9), 1691–1696.
585 <https://doi.org/10.1002/grl.50269>
- 586 Nishida, K., & Takagi, R. (2016). Teleseismic S wave microseisms. *Science*, *353*(6302), 919–
587 921. <https://doi.org/10.1126/science.aaf7573>
- 588 Obrebski, M. J., Arduin, F., Stutzmann, E., & Schimmel, M. (2012). How moderate sea states
589 can generate loud seismic noise in the deep ocean. *Geophysical Research Letters*, *39*(11),
590 1–6. <https://doi.org/10.1029/2012GL051896>
- 591 Phạm, T. S., Tkalčić, H., Sambridge, M., & Kennett, B. L. N. (2018). Earth's Correlation
592 Wavefield: Late Coda Correlation. *Geophysical Research Letters*, *45*(7), 3035–3042.
593 <https://doi.org/10.1002/2018GL077244>
- 594 Peterson, J. (1993). *Observations and Modeling of Seismic Background Noise*. *U.S. Geol. Surv.*
595 *Open File Report 93-322*. <https://doi.org/10.3133/ofr93322>
- 596 Poli, P., Thomas, C., Campillo, M., & Pedersen, H. A. (2015). Imaging the D'' reflector with
597 noise correlations. *Geophysical Research Letters*, *42*(1), 60–65.
598 <https://doi.org/10.1002/2014GL062198>

- 599 Rascle, N., & Arduin, F. (2013). A global wave parameter database for geophysical
600 applications. Part 2: Model validation with improved source term parameterization.
601 *Ocean Modelling*, 70, 174–188. <https://doi.org/10.1016/j.ocemod.2012.12.001>
- 602 Retailleau, L., & Gualtieri, L. (2019). Toward high-resolution period-dependent seismic
603 monitoring of tropical cyclones. *Geophysical Research Letters*, 46(3), 1329–1337.
604 <https://doi.org/10.1029/2018GL080785>
- 605 Rost, S., & Thomas, C. (2002). Array seismology: Methods and applications. *Reviews of*
606 *Geophysics*, 40(3), 1008. <https://doi.org/10.1029/2000RG000100>
- 607 Shapiro, N. M., & Campillo, M. (2004). Emergence of broadband Rayleigh waves from
608 correlations of the ambient seismic noise. *Geophysical Research Letters*, 31(7), 8–11.
609 <https://doi.org/10.1029/2004GL019491>
- 610 Spica, Z., Perton, M., & Beroza, G. C. (2017). Lateral heterogeneity imaged by small-aperture
611 ScS retrieval from the ambient seismic field. *Geophysical Research Letters*, 44(16),
612 8276–8284. <https://doi.org/10.1002/2017GL073230>
- 613 Stehly, L., Campillo, M., & Shapiro, N. M. (2006). A study of the seismic noise from its long-
614 range correlation properties. *Journal of Geophysical Research*, 111(B10), B10306.
615 <https://doi.org/10.1029/2005JB004237>
- 616 Steim, J. M. (2015). Theory and Observations - Instrumentation for Global and Regional
617 Seismology. In *Treatise on Geophysics* (pp. 29–78). Elsevier.
618 <https://doi.org/10.1016/B978-0-444-53802-4.00023-3>
- 619 Stutzmann, E., Arduin, F., Schimmel, M., Mangeney, A., & Patau, G. (2012). Modelling long-
620 term seismic noise in various environments. *Geophysical Journal International*, 191(2),
621 707–722. <https://doi.org/10.1111/j.1365-246X.2012.05638.x>
- 622 Stutzmann, E., Schimmel, M., Patau, G., & Maggi, A. (2009). Global climate imprint on seismic
623 noise. *Geochemistry, Geophysics, Geosystems*, 10(11), Q11004.
624 <https://doi.org/10.1029/2009GC002619>
- 625 Xia, H. H., Song, X., & Wang, T. (2016). Extraction of triplicated PKP phases from noise
626 correlations. *Geophysical Journal International*, 205(1), 499–508.
627 <https://doi.org/10.1093/gji/ggw015>
- 628 Ying, Y., Bean, C. J., & Bromirski, P. D. (2014). Propagation of microseisms from the deep
629 ocean to land. *Geophysical Research Letters*, 41(18), 6374–6379.
630 <https://doi.org/10.1002/2014GL060979>
- 631 Zhang, J., Gerstoft, P., & Shearer, P. M. (2010). Resolving P-wave travel-time anomalies using
632 seismic array observations of oceanic storms. *Earth and Planetary Science Letters*,
633 292(3–4), 419–427. <https://doi.org/10.1016/j.epsl.2010.02.014>

634

1

2

[Geochemistry, Geophysics, Geosystems]

3

Supporting Information for

4

Spatiotemporal correlation analysis of noise-derived seismic body waves with ocean wave climate and microseism sources

5

6

Lei Li¹, Pierre Boué¹, Lise Retailleau², Michel Campillo¹

7

¹Univ. Grenoble Alpes, Univ. Savoie Mont Blanc, CNRS, IRD, IFSTTAR, ISTerre, 38000 Grenoble, France

8

²Observatoire Volcanologique du Piton de la Fournaise, IPGP, CNRS, UMR 7154-Sismologie, La Plaine des Cafres, La Réunion, France

9

10

Contents of this file

12

Text S1 to S4

13

Figures S1 to S4

14

15

Additional Supporting Information (Files uploaded separately)

17

Caption for Movie S1

18

19

S1. FNET-LAPNET noise correlations

20

The correlation function C_{AB} between two seismograms (S_A and S_B) is given by

21

$$C_{AB}(\tau) = \frac{\sum_i S_A(i) S_B(i-\tau)}{\sqrt{\sum_i S_A^2(i) \sum_i S_B^2(i)}}. \quad (\text{S1})$$

22

The resultant C_{AB} consists of an acausal part and a causal part, that correspond to the negative lags ($\tau < 0$) and the positive lags ($\tau > 0$), respectively. For efficiency, it is routine to compute the correlation function with the Fast Fourier Transform:

23

24

25

$$C_{AB}(\tau) = \frac{\mathcal{F}^{-1}[\mathcal{F}(S_A)\mathcal{F}^*(S_B)]}{\sqrt{\sum_i S_A^2(i) \sum_i S_B^2(i)}}. \quad (\text{S2})$$

26

Figure S1(a) shows the acausal and causal sections of FNET-LAPNET noise correlations that are filtered between 5 s and 10 s and binned in distance intervals of 0.1° . The acausal section is flipped to share the time axis with the causal section. The expected locations of the acausal and causal noise sources are marked by stars on the maps of global microseism source PSDs and ocean wave heights in Fig. S1(b). The ocean wave activities and microseism excitations at the acausal source region are intense, while those in the

27

28

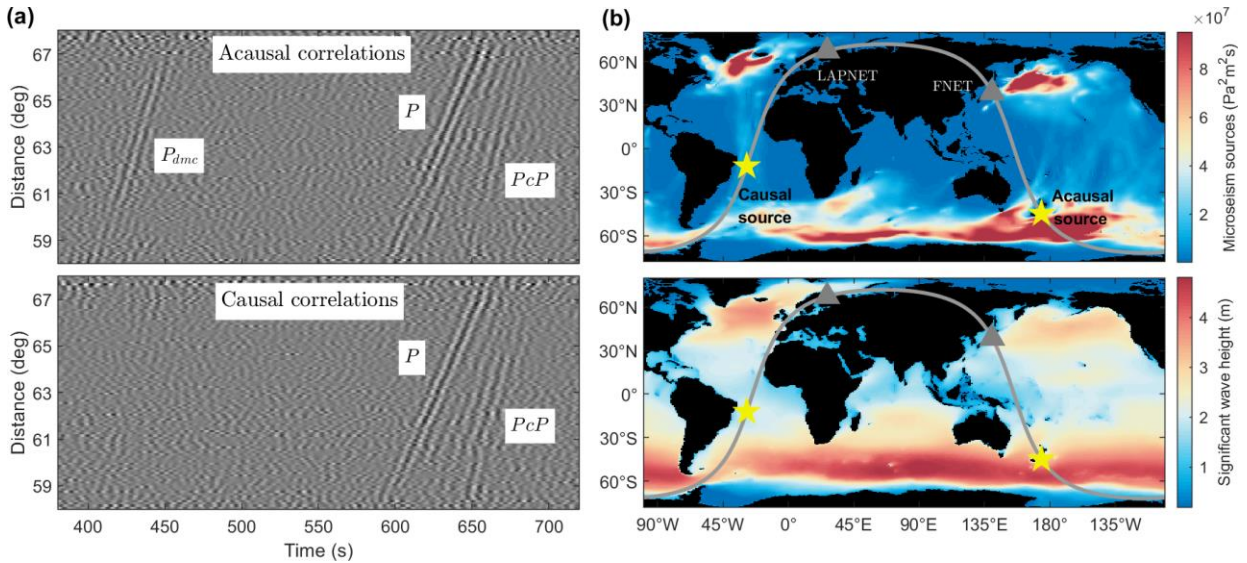
29

30

31

32

33 causal source region are fainter. Consequently, the P_{dmc} phase is only observable from the
 34 acausal noise correlations.
 35



36
 37 Figure S1. (a) Acausal and causal sections of FNET-LAPNET noise correlations. (b)
 38 Global maps of 6.2 s period secondary microseism sources and significant wave heights
 39 in 2008.

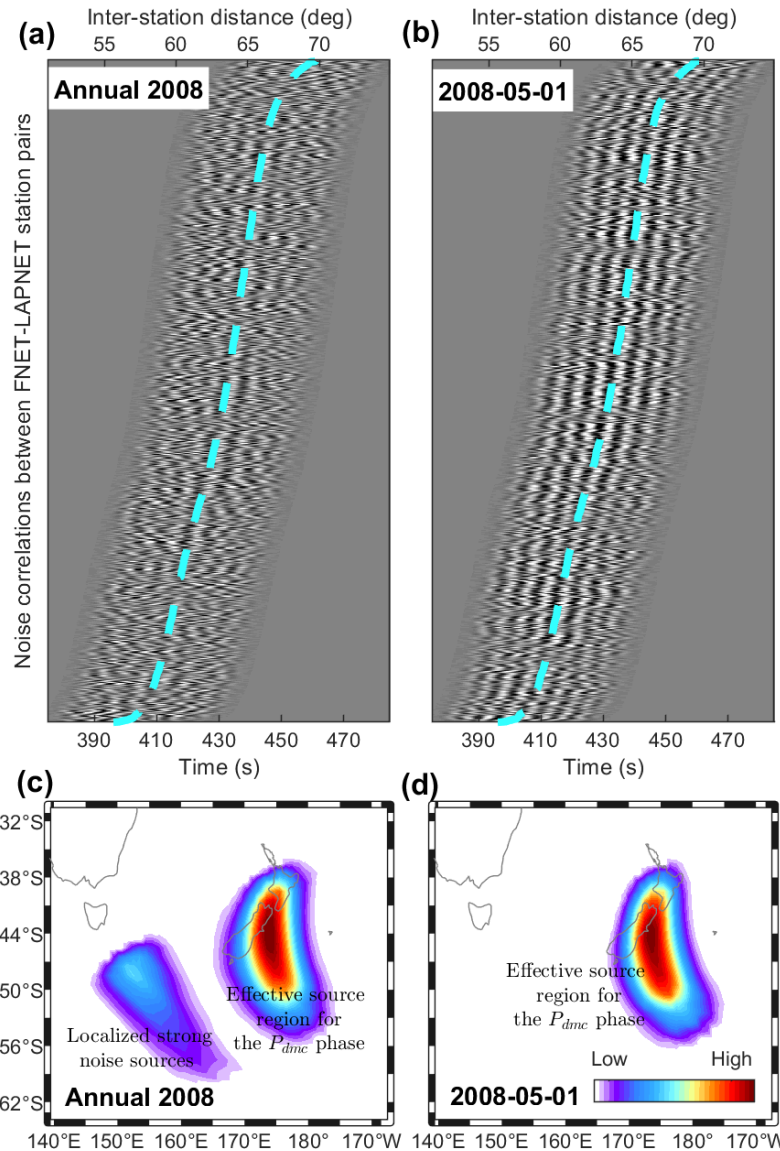
40

41 S2. Noise source imaging by back-projection

42 Assuming the interferometry between P waves at FNET and $PKPab$ waves at
 43 LAPNET, we image the effective noise sources through the back-projection of the
 44 FNET-LAPNET noise correlations. We beam the FNET-LAPNET noise correlations and
 45 assign the beam power

$$46 P_s = \langle \langle C_{ij}(t + t_{si} - t_{sj}) \rangle \rangle_{ij}^2, \quad (S3)$$

47 onto a $0.5^\circ \times 0.5^\circ$ grid as the probabilities of noise sources on the global surface. In the
 48 above equation, $\langle \cdot \rangle_x$ means the average over x , C_{ij} is the correlation function between the
 49 i -th FNET station and the j -th LAPNET station, t_{si} is the traveltime of the P wave from
 50 the s -th grid point to the i -th FNET station, and t_{sj} is the traveltime of the $PKPab$ waves
 51 from the s -th source to the j -th LAPNET station. The inter-station noise correlations are
 52 windowed before the beamforming (Fig. S2a). The noise source imaging for the annually
 53 stacked noise correlations is plotted in Fig. S2(c). Only the region surrounding NZ is
 54 shown. Outside the region, hardly can the P wave reach FNET or the $PKPab$ waves reach
 55 LAPNET. Besides a well-focused imaging of the expected source region in the ocean
 56 south of NZ, we notice a secondary spot to the west. In comparisons with the power map
 57 of oceanic microseism noise sources in Fig. 5(e), we ascribe it to the strong microseism
 58 excitation in the ocean south of Tasmania. We also back-project the daily noise
 59 correlations on 2008-05-01 (Fig. S2b), when the P_{dmc} phase reaches the largest strength
 60 through the year (Fig. 2). As shown in Fig. S2(d), an exclusive source region is imaged,
 61 which agrees with the dominant spot in Fig. S2(c).



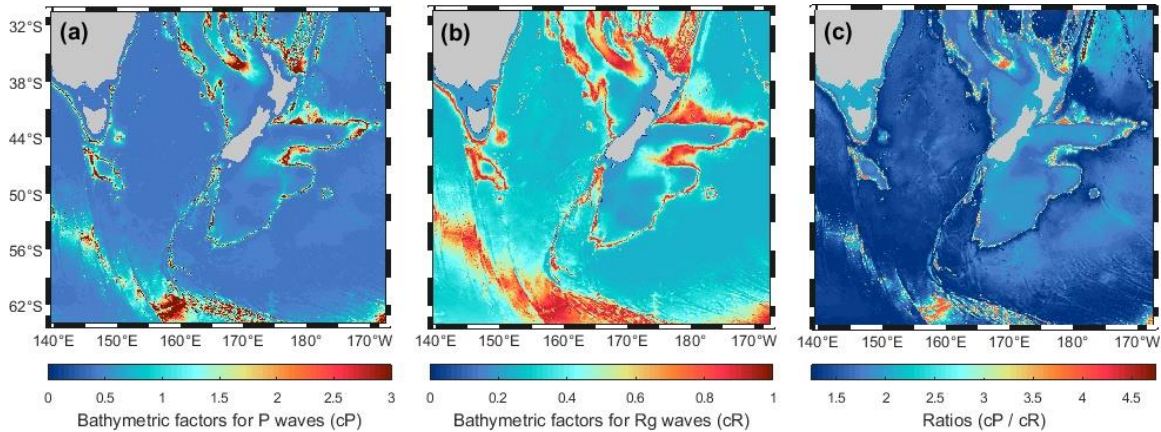
63
 64 Figure S2. Inter-receiver noise correlations for all FNET-LAPNET station pairs: (a)
 65 stacked over the year of 2008; (b) on single day of 2008-05-01. The waveforms are
 66 windowed around the P_{dmc} phase. Dashed lines indicate inter-station distances. Back-
 67 projection imaging of noise sources: (c) using data from (a); (d) using data from (b).

68

69 S3. Bathymetric amplification factors

70 Figure S3 compares the bathymetric amplification factors surrounding New
 71 Zealand for P waves and Rayleigh waves. The factors for P waves are computed using
 72 the equations proposed by Gualtieri et al. (2014), for a seismic period of 6.2 s and a
 73 slowness of 4.6 s/deg. The factors for 6.2 s period Rayleigh waves are obtained by
 74 interpolating the table given by Longuet-Higgins (1950).

75



76
 77 Figure S3. Bathymetric amplification factors for (a) P waves and (b) Rayleigh waves. (c)
 78 Ratios between the factors for P waves and for Rayleigh waves.

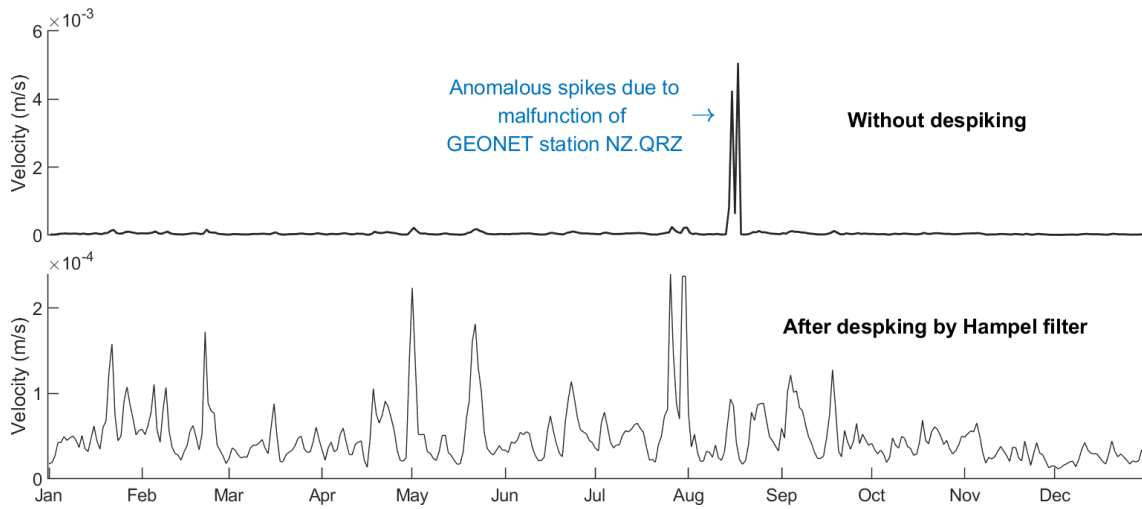
79

80 S4. Microseism noise levels at seismic networks

81 The continuous seismograms record not only the background vibrations of Earth, but
 82 also ground motions induced by seismicity or other events. Instrumental malfunction also
 83 leads to anomalous (e.g., nearly vanishing or extremely large) amplitudes in the records.
 84 These extreme amplitudes (outliers) could bias the estimates of microseism noise power.
 85 It is necessary to get rid of them from the ambient noise records before the computation
 86 of noise power. Mean and median filters are the common tools for this task. However,
 87 they modify all the samples. Here, we prefer to use a variant of the median filter called
 88 Hampel filter. In contrast to the median filter that replace all samples with local medians,
 89 the Hampel filter detects outliers by compare a sample with the neighboring samples. A
 90 sample is replaced by the local median if it deviates k times of the median absolute
 91 deviation (MAD) from the local median, or else, it is unchanged.

92 We filter the vertical components of the continuous seismograms around 6.2 s
 93 period. The seismograms are then divided into 15-min segments and the power of
 94 segments is computed. We apply the Hampel filter to the time series of noise power
 95 recursively. For each sample, we compute the local median and MAD of its eight
 96 neighbors (four before and four after). A sample is replaced by the median if it deviates
 97 from the median over three times of the MAD. The de-spiked time series is resampled
 98 from a 15-min interval to a 1-hour interval, by averaging over every four samples. Then,
 99 we apply the Hampel filter again and resample the time series to a 24-hour interval. The
 100 averaging of noise levels over all stations of a seismic network leads to the time series of
 101 array noise level. Before the averaging, the Hampel filter is applied again, to discard
 102 possible anomalous values at some stations (see Fig. S3 for the example of GEONET).
 103 The final time series of microseism noise levels for networks FNET, LAPNET and
 104 GEONET are shown in Fig. 6.

105



106
107
108
109
110

Figure S4. Comparison between the time series of daily GEONET noise levels with (lower) and without (upper) despiking using the Hampel filter.

111
112
113

Movie S1. Daily evolutions of winds, ocean wave heights, and secondary microseism source PSDs around New Zealand in 2008.